Research Article

Experimental and Numerical Studies on Permeability Properties of Thermal Damaged Red Sandstone under Different Confining Pressures

Zhenlong Zhao, Hongwen Jing [ID], Guangping Fu, Qian Yin [ID], Xinshuai Shi, and Yuan Gao

State Key Laboratory for Geomechanics and Deep Underground Engineering, China University of Mining and Technology, Xuzhou 221116, China

Correspondence should be addressed to Hongwen Jing; tb18220025b4@cumt.edu.cn

The stability and safety of underground rock mass engineering are closely related to the permeability process of fluids and permeability properties of rocks. To reveal the flow behavior of fluid in thermal damaged rock, first, a rock seepage testing system was applied to study the permeability properties of red sandstone specimens after different high-temperature treatments from 200 to 800°C under different confining pressures of 10 to 30 MPa. Meanwhile, the microstructures of the red sandstone specimens were characterized by the mercury intrusion porosimetry (MIP) and scanning electron microscopy (SEM). Then, the permeability process of pore water pressure and the flow form of fluid also were investigated by the numerical modeling method. The results show that the permeability properties of red sandstone specimens after high-temperature exposure follow linear Darcy's law, and the relation between confining pressures and equivalent permeability coefficient (K_0) can be described by a power function. Besides, the phenomenon that microscopic structural deterioration is intensified with increasing temperature and the average pore size and porosity of the red sandstone specimens are both power functions is related to the equivalent permeability coefficient. Furthermore, the results of numerical modeling indicated that the flow field within the range affected by confining pressures gradually becomes stable and orderly from disorder, and flow lines of the fluid become smooth and straight, and perpendicular to the isosurface of pore water pressure as time goes by. Moreover, the nonlinear correlation between pore water pressure and seepage path length changes to a linear correlation, which is consistent with linear Darcy's law.

1. Introduction

With the development of geothermal energy, coal mining, nuclear waste treatment, and underground coal gasification, as well as the restoration of underground protection engineering, various problems are more and more prominent [1–4]. One of the problems is the change of physical and mechanical properties of surrounding rock mass caused by thermal damage, especially the evolution process of permeability characteristics of rocks after high-temperature exposure has become a hot topic in the fields of rock thermodynamics and hydraulics [5–11]. The permeability properties of the rocks are the basic parameters in rock hydraulics [12].

Studies have shown that high temperature causes changes in the microstructure of rocks by inducing thermal damage phenomena such as the initiation, propagation, and coalescence of microcracks, which directly affects the permeability properties of rocks [13–18]. To solve this problem, Dwivedi et al. [19] summarized five main mechanical parameters of granite after high-temperature exposure by studying various thermodynamic behaviors of Indian granite under high temperature, providing information for the study of the thermodynamic mechanism of granite. Griffiths et al. [20] and Freire-Lista et al. [21] used various methods to study the crack growth of granite after high-temperature exposure, and the results showed that when the temperature was lower than 400°C, the permeability of sandstone decreased slowly
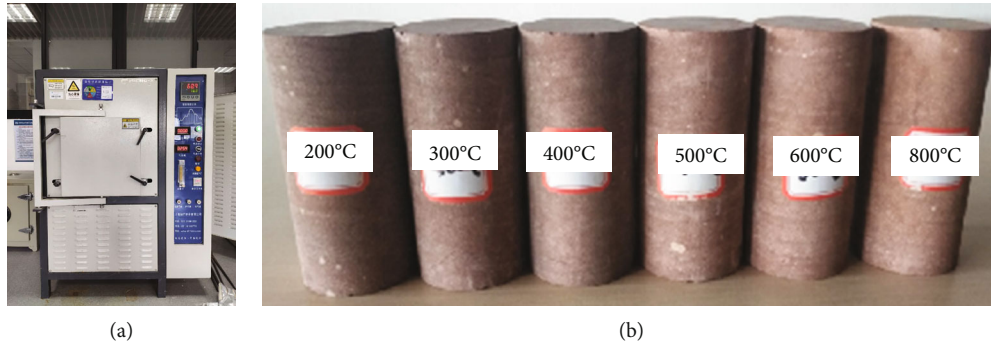
FIGURE 1: Specimen preparation. (a) The high-temperature furnace. (b) The red sandstone specimens after high-temperature exposure.
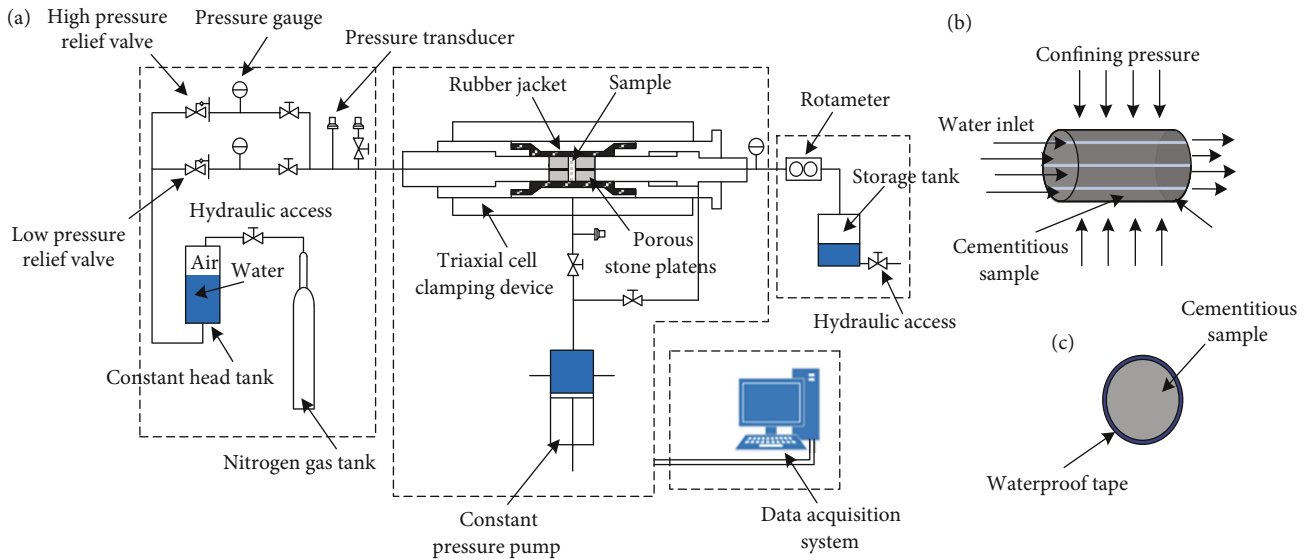

FIGURE 2: Schematic diagram of seepage testing system [11].

with the increasing temperature, while when the temperature increased from 400 to 600°C, the permeability of sandstone increased rapidly with the increasing temperature. Chaki et al. [22]. Ma et al. [23] believed that the permeability was greatly affected by the total porosity, effective porosity, and critical pore size of the specimen. Chen et al. [24] studied the relationship between permeability properties of granite and temperatures, and the results showed that when the temperature was less than 300°C, the permeability changed slightly, when the temperature increased from 300 to 500°C, the permeability increased gradually, and when the temperature was greater than 500°C, the permeability increased significantly. Gao et al. [25] carried out permeability and the mercury intrusion porosimetry (MIP) tests and then used the fractal dimension of the pore characteristics of the sample to capture the correlation between the transport characteristics and the pore structure, so as to predict the permeability-related characteristics of the specimen. These studies mainly focus on the changes in microscopic morphology and permeability properties of rocks after high-temperature exposure. However, the permeability process of the rock under confining pressure is rarely reported. High temperature induces the generation and propagation

of cracks in rocks, thus, affecting the permeability properties of the rocks. Meanwhile, confining pressure also affects the permeability properties of the rocks. In addition, the relationship between the permeability and the porosity of rock has also been studied [22, 26–30]. Chaki et al. [22] studied the porosity and permeability evolutions of thermal damage granite, and results showed that the permeability measurement can better characterize the porosity and connected porosity of the specimen. Jiang et al. [26] established a new wave velocity-permeability model for granite subjected to different temperatures according to the modified wave velocity-porosity formula and Kozeny-Carman formula. Jia et al. [27] and Zheng et al. [28] studied the effective stress-dependent permeability and porosity of low-permeability rock, and results showed that a power-law form can be used to describe the correlation of permeability and porosity.

These studies are useful for understanding the permeability characteristics of rocks. However, there are few studies on the relationship between the microscopic physical properties and the macroscopic permeability characteristics under different confining pressures by characterizing the characteristics of thermal damaged red sandstone from the perspective of the mercury intrusion porosimetry and scanning electron
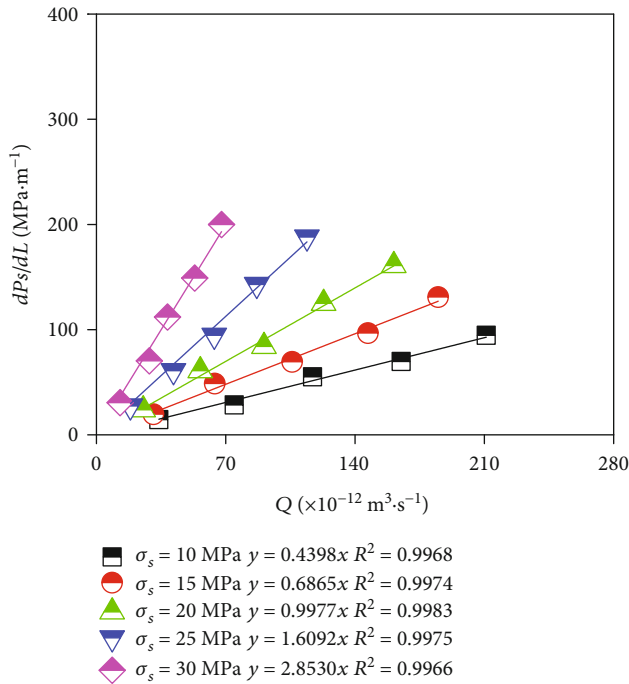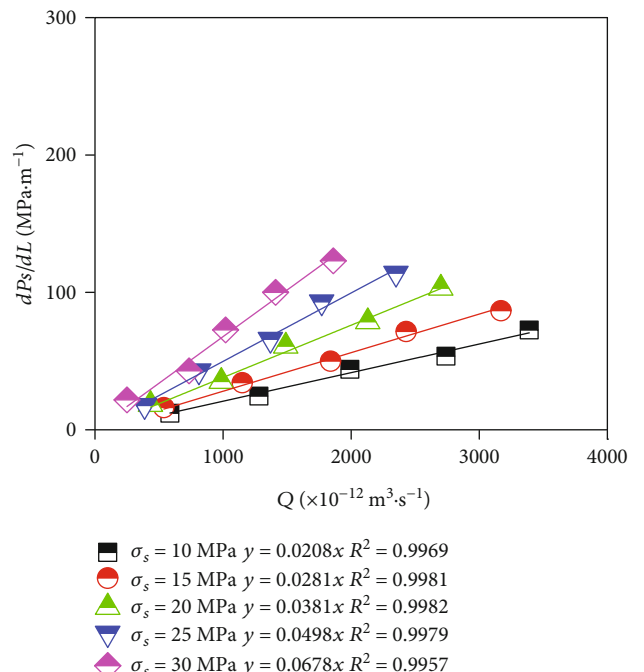
(a)
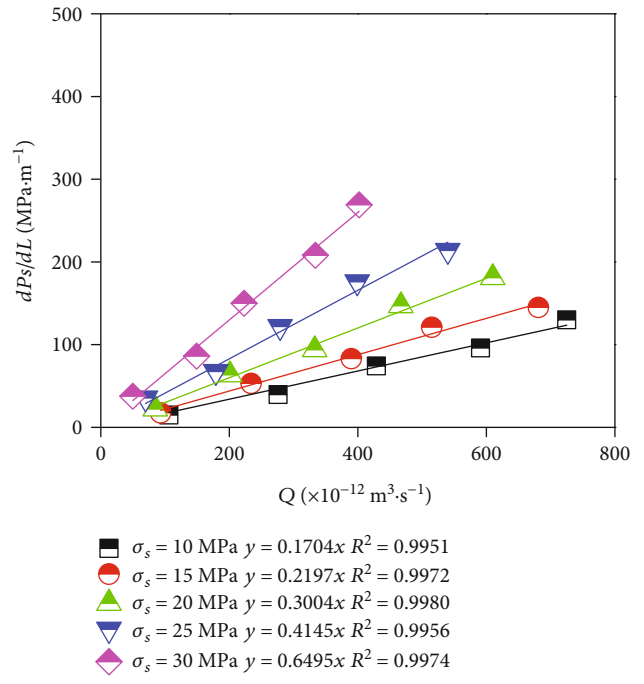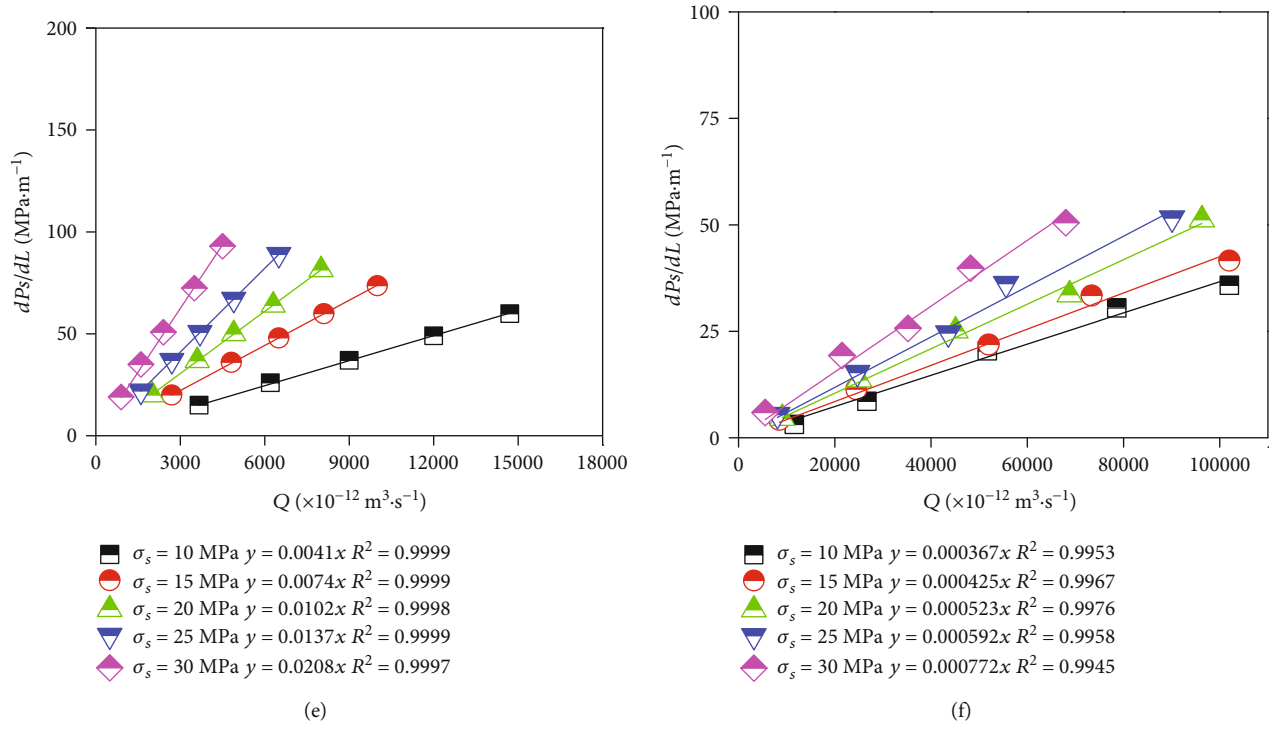
(b)
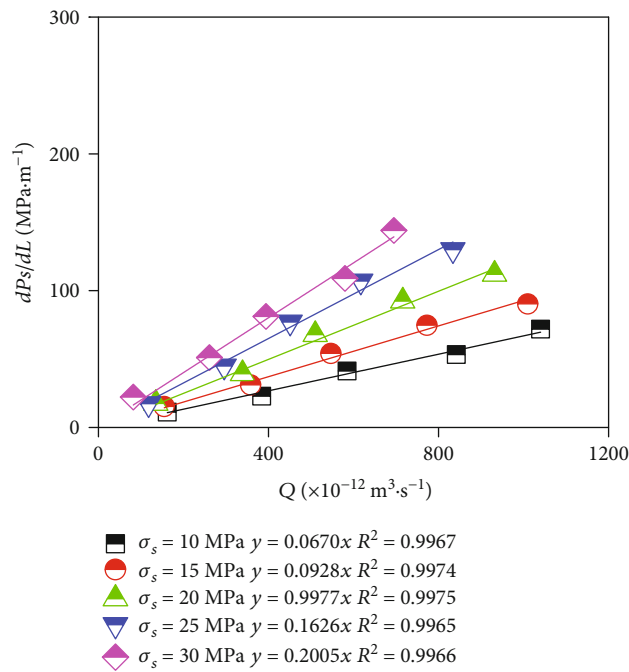
(c)

(d)

Figure 3: Continued.

(e)

(f)

Figure 3: Relationship between volume velocity and pressure gradient.

Table 1: Equivalent permeability coefficient of red sandstone specimens at different temperatures and confining pressures ($\times 10^{-18}$ m^2).

σ_s (MPa)	T (°C)					
	200	300	400	500	600	800
10	1.16	3.00	7.61	24.52	124.40	1389.65
15	0.74	2.32	5.50	18.51	68.92	1200.00
20	0.51	1.70	4.10	13.39	50.00	975.14
25	0.32	1.23	3.14	10.24	37.23	861.49
30	0.18	0.79	2.54	7.52	24.52	660.62

microscopy (SEM). Thus, to reveal the correlation between permeability characteristics of thermal damaged red sandstone and confining pressure, first, the permeability properties of red sandstone specimens after high-temperature exposure of 200, 300, 400, 500, 600, and 800°C were studied under different confining pressures of 10, 15, 20, 25, and 30 MPa. Then, the microstructures of the red sandstone specimens were characterized by the mercury intrusion porosimetry and scanning electron microscopy. Moreover, the permeability process of pore water pressure and the flow form of fluid were further investigated by numerical modeling method.

2. Methodology

2.1. Specimen Preparation. The natural red sandstones in this study are all from Laizhou Mining Area, Shandong Province, China. There are no visible textures and cracks on the surface, and the structure is complete. In the natural state, the
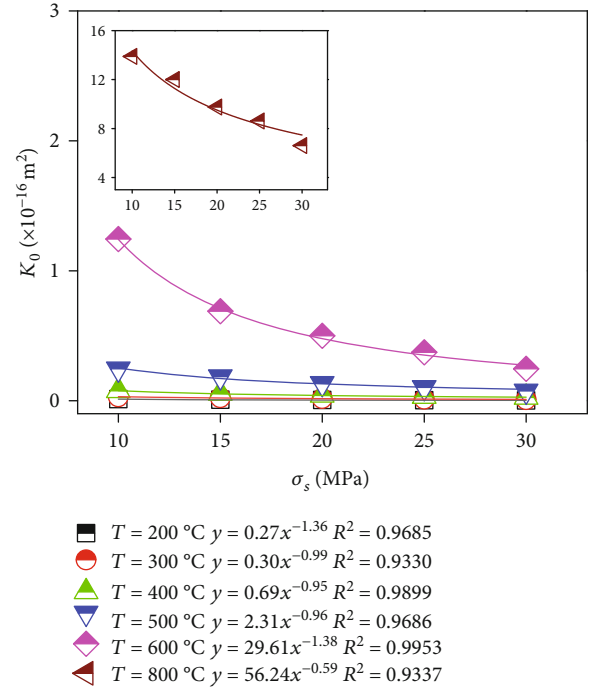

Figure 4: Relationship between equivalent permeability coefficients and confining pressures.

rocks are reddish brown. The main components are quartz, feldspar, and illite, with an average density of 2.47 g·cm^{-3}. The complete red sandstone blocks were cored, cut, and polished into a standard cylindrical specimen with a diameter of 50 mm and a height of 100 mm as recommended by

TABLE 2: Pore structure parameters of heat-treated red sandstone specimens.

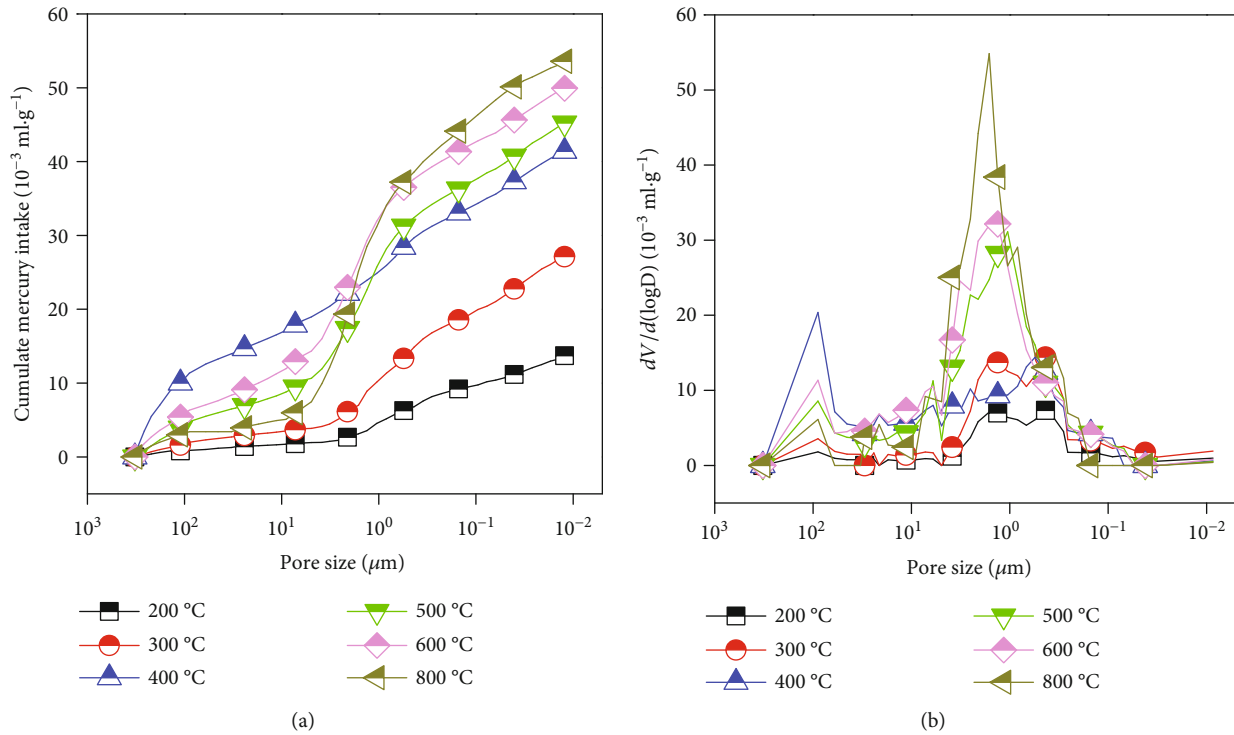| Parameters	T (°C)					
	200	300	400	500	600	800
Cumulative mercury intake (ml·g^{-1})	0.0146	0.0287	0.0448	0.0468	0.0518	0.0544
Mean pore size (nm)	56.4	61.9	63.2	96.2	102.2	144.3
Porosity (%)	3.17	6.83	10.11	10.47	11.53	12.06

(a)

(b)

FIGURE 5: Pore structure of heat-treated red sandstone. (a) The relationship between the cumulative mercury intake of red sandstone under different pore sizes. (b) The distribution of pore structure.

the International Society for Rock Mechanics (ISRM) [31]. The height deviation of the specimens was within ±0.05 mm, and the allowable deviation of nonparallelism of the two end faces was ±0.02 mm. The mean uniaxial compressive strength of the specimens is 58.63 MPa obtained by an electrohydraulic servo testing machine. The red sandstone specimens were heat-treated by a high-temperature furnace, as shown in Figure 1(a).

To revel the influence of temperatures on the properties of red sandstone, the target temperatures were set at 200, 300, 400, 500, 600, and 800°C, respectively, and the heating rate was 10°C·min^{-1} [32]. When the temperature reached the designed temperature, keep the high temperature for 150 min, so that the heat could be fully transmitted within the specimens. Then, the specimens were taken out for natural cooling. The cooled specimens were wrapped with plastic film to prevent the influence of humidity in the air. The red sandstone specimens after high-temperature exposure were shown in Figure 1(b).

2.2. Experimental Process. The full-automatic seepage testing system in the State Key Laboratory for Geomechanics and

Deep Underground Engineering, China University of Mining and Technology was used to carry out permeability tests on red sandstone specimens after high-temperature exposure. The schematic diagram of the testing system is shown in Figure 2. The testing system is mainly composed of water inlet subsystem, triaxial seepage test subsystem, and data acquisition subsystem, and the maximum confining pressure of 60 MPa can be applied to the specimens. The data in the test process are automatically saved by the data acquisition subsystem.

First, the specimens were immersed in distilled water, and when the weight of the specimens was constant, the specimens were considered to be saturated before the test. Then, the specimens were wrapped with 3 mm waterproof tape, and the waterproof tape was smooth and covered the surfaces of the specimens, so as to prevent the test error caused by water overflow and uneven distribution of confining pressure. The wrapped specimen was put into the container of the triaxial seepage test subsystem along the axial horizontal direction. To ensure the uniform distribution of water pressure, a porous metal gasket was placed at both ends of the axial direction of the specimen. Meanwhile, a lower confining
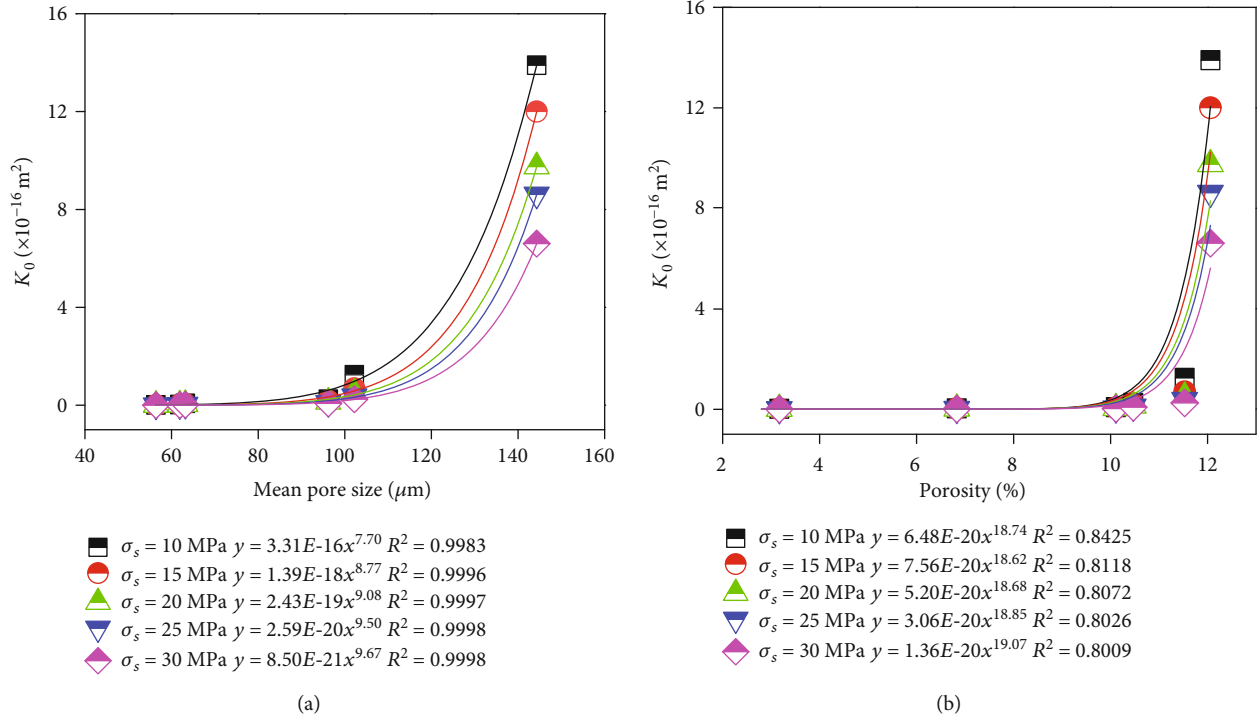
FIGURE 6: Relation of equivalent permeability coefficient with mean pore size and porosity.

pressure was applied, and an initial water inlet pressure was set to prevent test error. When the outlet flow velocity is stable, the confining pressure was set to 10, 15, 20, 25, and 30 MPa, respectively. When the confining pressure reached to predetermined value, the outlet pressure was controlled by the cross-flow pump and gradually increased. The inlet and outlet pressures can be recorded through the pressure gauge and stored on the computer with an accuracy of 0.01 MPa. When the flow rate through the specimen is stable, the permeability coefficient can be calculated through real-time data, so as to quantitatively evaluate the influence of confining pressure and temperatures on the permeability characteristics of the red sandstone specimen.

3. Results and Discussion

3.1. Permeability Properties. The relationship between axial hydraulic gradient and volumetric velocity is shown in Figure 3. It is clear that with the increasing volumetric velocity, the axial hydraulic gradient increases, and the axial hydraulic gradient under the same confining pressure has a linear correlation with the volume velocity, and the correlation coefficients are greater than 0.99, indicating that the permeability of red sandstone after high-temperature exposure can be well characterized by linear Darcy's law. In addition, with the increasing confining pressure, the fitting line changes steep slope, showing that high confining pressure makes the seepage channel gradually narrowed and increases the resistance of fluid migration to hold back the flow of the fluid. It also can be seen from the effect of temperature on fitting line slope under the same confining pressure that temperature has a great influence on the permeability properties of the specimens.

Considering that the equivalent permeability coefficient is an important parameter to evaluate the permeability of rocks [4, 25, 33, 34], and assuming that water is an incompressible fluid, the equivalent permeability coefficient can be described as a linear function of zero intercept in linear Darcy's Law [35].

$$K_0 = \frac{\mu}{A_0} \frac{dL}{dP_S} Q, \tag{1}$$

where K_0 is the equivalent permeability coefficient, μ is hydraulic viscosity coefficient and 10^{-3} Pa·s in this paper, A_0 is the cross-section area of the specimens and 1.96×10^{-3} m^2 in this paper, P_s is the pressure difference between inlet and outlet water, and L is the length of specimen and 0.1 m in this paper. The equivalent permeability coefficient of red sandstone specimens with different temperature levels and confining pressures was calculated and analyzed as shown in Table 1.

Table 1 shows the change of equivalent permeability coefficient under different temperatures and confining pressures. Clearly, high temperature can improve the equivalent permeability coefficient of the specimens, and the equivalent permeability coefficient increases several times over with the increasing temperature, which is similar to the permeability characteristics of granite after high-temperature exposure obtained by Chen et al. [24]. The equivalent permeability coefficient is the smallest at 200°C at the same confining pressure. When the temperature is 800°C, the equivalent
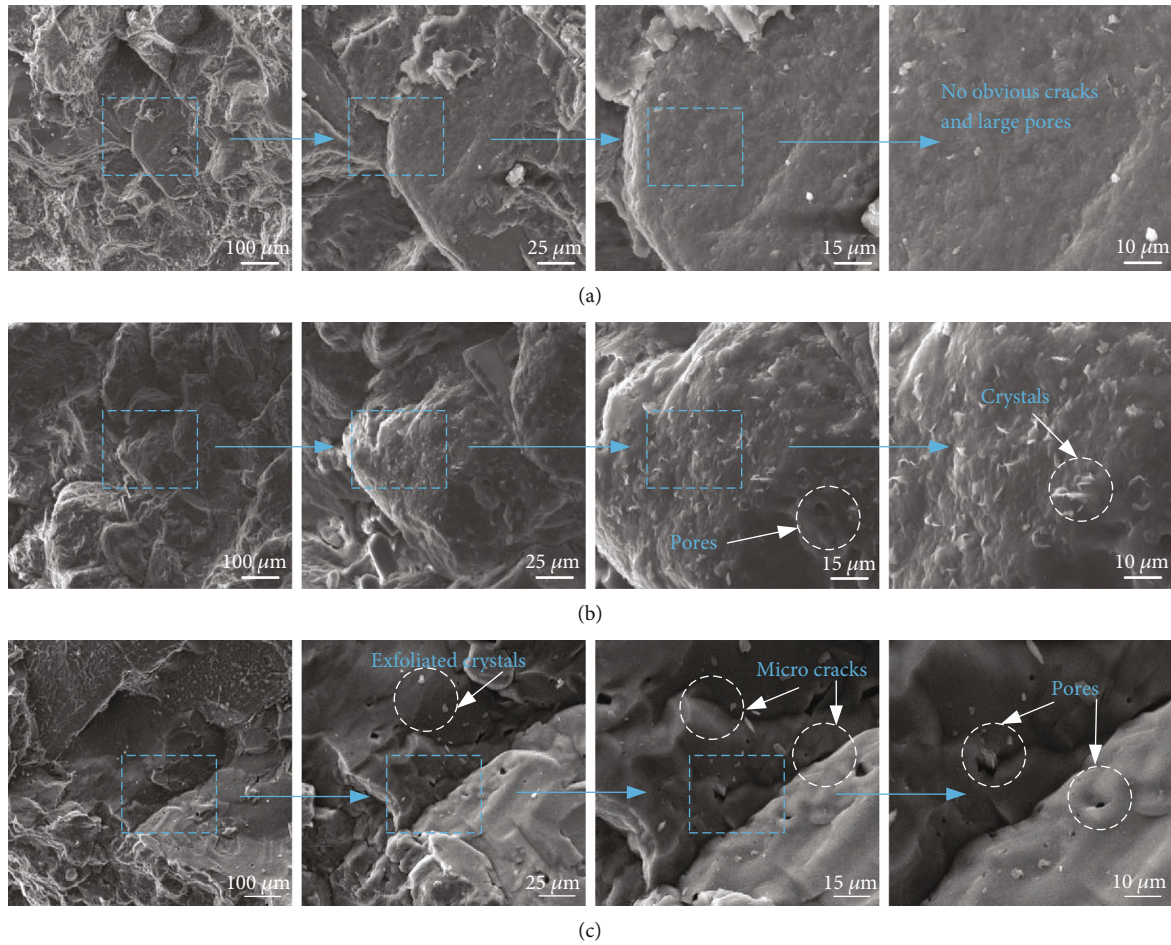
(a)

(b)

(c)

FIGURE 7: Scanning electron microscopy image of red sandstone surface before and after heat treatment.
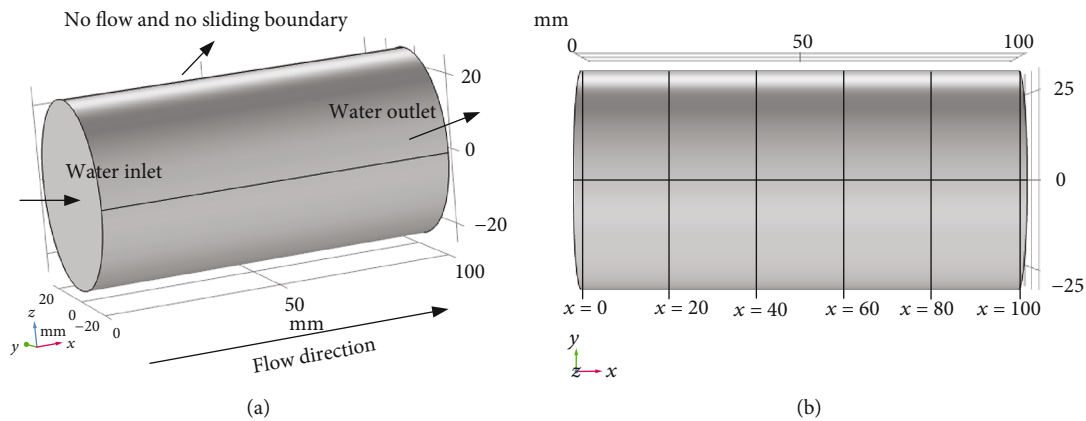

(a)

(b)

FIGURE 8: Seepage model. (a) Seepage model of heat-treated red sandstone. (b) Section division of the seepage path length division.

permeability coefficient reaches the maximum value and much higher than other temperatures. When the temperature increases from 200 to 800°C, the equivalent permeability coefficient increases by $659.82 \times 10^{-18} - 1388.49 \times 10^{-18}$ m^2. In addition, when the confining pressure increases from 10 to 30 MPa, the equivalent permeability coefficient decreases by 52.5–84.5%. Figure 4 further shows the equivalent permeability coefficient and confining pressure. When the temper-

ature is 200°C, the fitting variable is 0.27. When the temperature is 800°C, the fitting variable is 56.24, increasing 207 times compared to 200°C, which indicates that the higher the temperature makes the permeability increase.

3.2. Pore Structure Characteristics. The permeability properties of rocks are closely related to the microstructure such as pore size, distribution, and connectivity. Thus, the
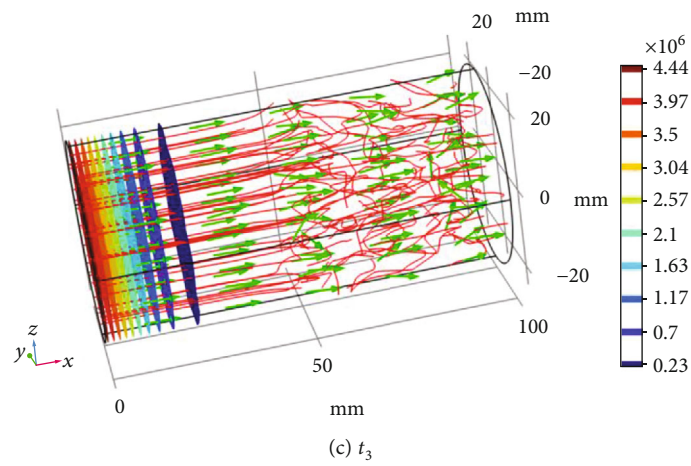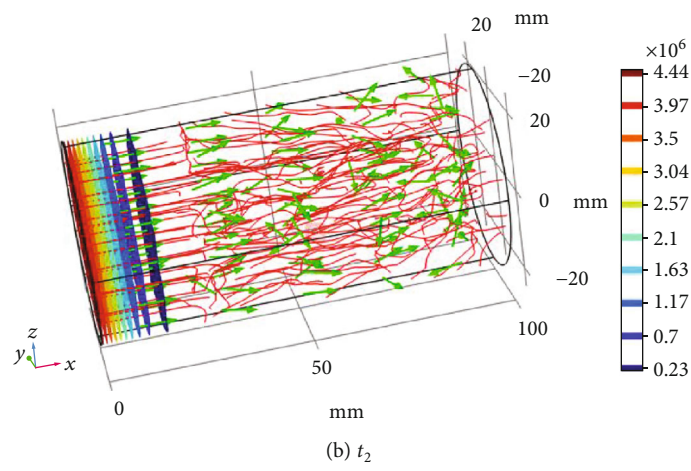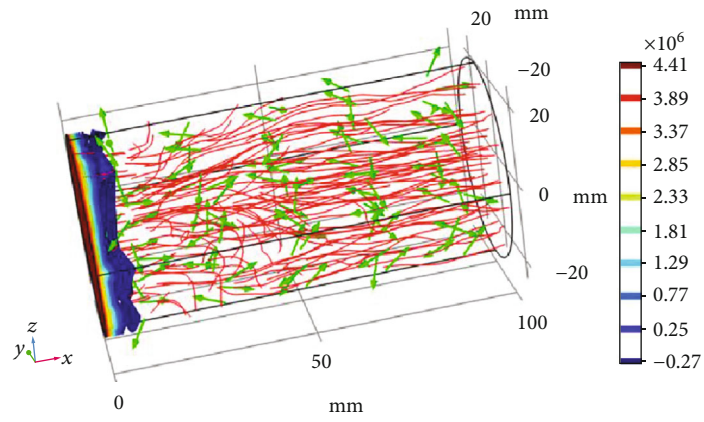
(a) t_1

(b) t_2

(c) t_3

Figure 9: Continued.
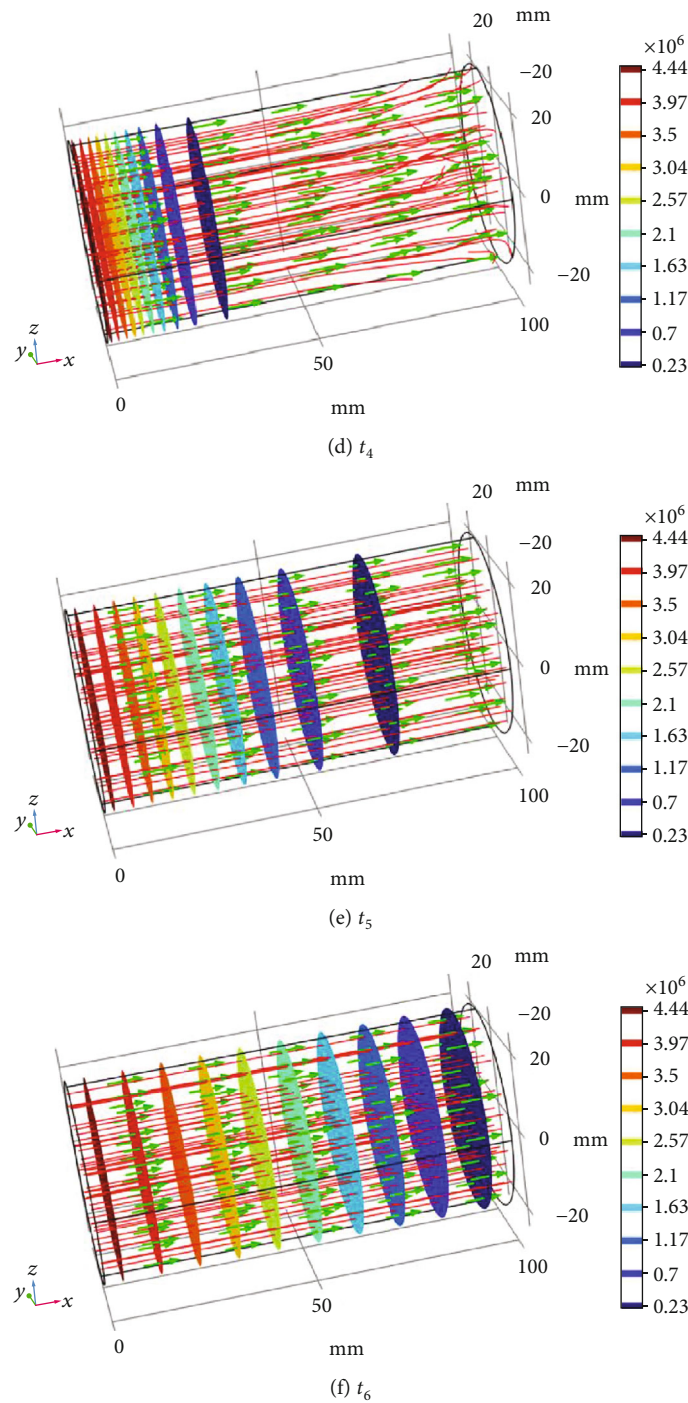
(d) t_4

(e) t_5

(f) t_6

FIGURE 9: Relationship between pore water pressure and flow field over time.

mercury intrusion porosimetry was adopted to test the pore structure of red sandstone after high-temperature exposure. The test results are shown in Table 2. The relationship between the cumulative mercury intake under different pore sizes and the pore distribution of pore structure are shown in Figure 5.

As we can see from Figure 5(a), with the increasing temperature, the accumulative mercury intake increases. When the temperature is 200°C, the mercury content, average pore diameter, and porosity of the specimens are the minimum. However, when the temperature increases from 200 to 800°C, the mercury content, average pore size, and porosity of the specimens increases by 2.7, 1.6, and 2.8 times, respectively. In particular, the curves of cumulative mercury intake at 300 and 400°C were far apart, indicating that when the temperature increased from 300 to 400°C, the pore structure of the specimens changed greatly. Moreover, when the pore diameter is less than 1.6 μm, the cumulative mercury intake of the specimens at 400°C reached the maximum, and the pore diameter is larger than 1.6 μm, the cumulative mercury

intake of the specimens at 800°C reached the maximum. Besides, it is clear in Figure 5(b) that there are two obvious peaks in the pore size distribution curve, and the highest peak appears when the pore diameter is $1\,\mu$m. After high temperature, the pore size of red sandstone is mainly distributed in the range of 0.1–$10\,\mu$m, mainly because of the mismatching of thermal expansion of different minerals and the temperature stress generated by anisotropy. Thermal fracture occurs inside red sandstone, leading to the increase of the diameter of primary pore fractures and the emergence of new pores. The other peak occurs at a pore diameter of $100\,\mu$m, and the maximum peak is at a temperature of 400°C, indicating that the red sandstone specimen at 400°C has more pores and a larger average pore diameter within this pore diameter range.

To better understand the influence of the equivalent permeability coefficient of red sandstone after high-temperature exposure, the relationship between average pore size and porosity and equivalent permeability coefficient is shown in Figure 6. It can be seen that the relationship of the equivalent permeability coefficient and both the average pore size and porosity can be described by the power function. In addition, the goodness of fit is 0.8009–0.9998 under different confining pressures, indicating that the porosity and pore diameter distribution are important factors affecting the permeability of water.

The red sandstone specimens at room temperature (25°C) and high temperature (400°C, 800°C) were observed by scanning electron microscopy, as shown in Figure 7. When the temperature is 25°C, the surface of the red sandstone specimen is relatively flat without visible cracks and large pores (Figure 7(a)). When the temperature rises to 400°C, pores gradually appear. The main reason is that the weak clay minerals begin to expand strongly at 400°C, leading to a sharp increase in microscopic defects. In addition, the development of cracks and pores under the influence of high temperature result in obvious heterogeneity, and the crystal particles begin to dissolve and break, showing irregular shapes and attached to the surface of the specimen (Figure 7(b)). When the temperature rises to 800°C, the crystal particles on the surface of the specimen exfoliate, the pores continue to develop and increase, and the microcracks and microdefects increase (Figure 7(c)).

3.3. Permeability Process of Pore Water Pressure.

In recent years, with the development of computer technology, the numerical modeling method has been widely used in the study of geotechnical engineering [36, 37]. COMSOL Multiphysics as a finite element numerical modeling method has a wide range of applications in many fields, including structural mechanics, fluid mechanics, and geotechnical mechanics. After high temperature, the pores and cracks in red sandstone increase, which directly affects the permeability of red sandstone specimens. Therefore, COMSOL Multiphysics numerical modeling software was adopted to simulate the permeability process of red sandstone after high-temperature exposure.

In this paper, the fluid module is selected, and the modeling process can be summarized into five steps: (1) the selection of the mass conservation principle in the seepage model, (2) the assumption of seepage physical field, (3) the
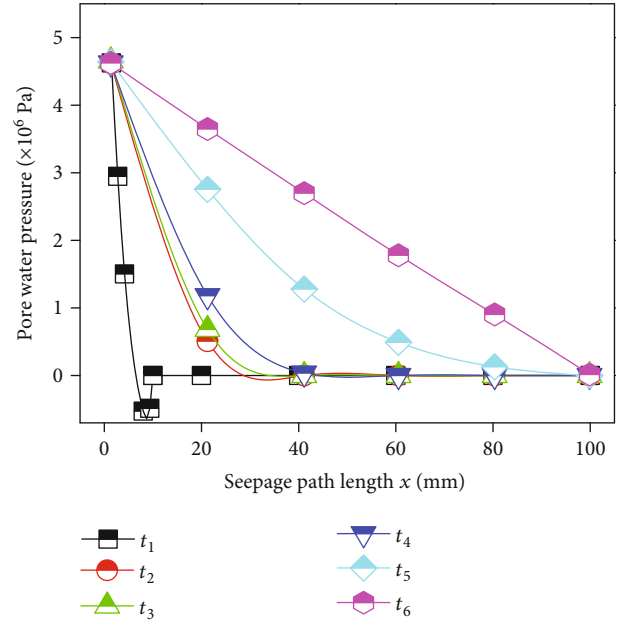

FIGURE 10: Relationship between pore water pressure and seepage path length.

establishment of the initial model based on the experimental results, (4) the assignment of model boundary conditions, and (5) data monitoring of model seepage process [38].

The mass conservation principle of the seepage model is expressed as:

$$\frac{\partial}{\partial t}\left(\varepsilon_p \rho\right) + \nabla(\rho u) = Q_m, \tag{2}$$

$$u = -\frac{k}{\mu}\nabla p, \tag{3}$$

where ρ is the density of fluid, u is the Darcy velocity vector, ∇p is the pressure gradient, μ is the dynamic viscosity coefficient, k is permeability coefficient, and ε_p is the porosity. According to the principle of conservation of mass, the mass of inlet water is equal to that of outlet water. The pressure gradient of the fluid is influenced by the permeability coefficient and porosity.

In addition, the boundary around the cylinder wall was set as no flow and no slip. In addition, Darcy's law was chosen as the physical field, assuming that (1) the sample is a homogeneous, isotropic linear elastomer, (2) the behavior of fluid flow is linear and can be described by Darcy's law, and (3) the fluid density and viscosity coefficient are constant, taking $1000\,\text{kg·m}^{-3}$ and $0.001\,\text{Pa·s}$, respectively.

The basic physical parameters of red sandstone specimens with the temperature of 800°C and confining pressure of 20 MPa were used for modeling. The equivalent permeability coefficient was set $975.14 \times 10^{-18}\,\text{m}^2$, the water inlet was set 4.67 MPa, the outlet pressure was set 0, and the porosity was set at 12.06%. By entering specific values in the interactive interface, COMSOL can automatically convert corresponding data into the above formulas based on the

programming language built into the fluid module. To better observe the influence of inlet pressure gradient on permeability behavior, the influence of confining pressure gradient is not taken into account. A standard cylinder model with a diameter of 50 mm and a height of 100 mm is established as shown in Figure 8(a).

The relationship between pore water pressure and flow field over time is shown in Figure 9. At the time t_1, the pore water pressure surface gathers at the water inlet, and the flow field inside the model is disordered because the pore water pressure has not been transferred to the interior of the model. At the time t_2, the pore water pressure surface moves forward further along the x-axis direction, and the distance between the pore water pressure surfaces gradually expands. Meanwhile, the pressure gradient gradually forms near the water inlet, and the streamline of the fluid within the pressure influence range gradually becomes orderly. At the time t_3, t_4, and t_5, the spacing between the pore water pressure surfaces is further enlarged, and the streamline of the fluid within the pressure range becomes smooth and straight gradually and is perpendicular to the pore water pressure isosurface. At the time t_6, the flow field inside the model becomes stable and orderly. The streamline is already perpendicular to the pore pressure surface, and the pore water pressure surface presents an equidistant distribution, in line with the linear Darcy's law.

To further explore the relationship between pore water pressure and seepage path length, the seepage path length was divided at 20 mm intervals along the x-axis direction as shown in Figure 8(b). It can be seen from Figure 10 that before the model reaches steady-state, the pressure and the seepage path length show a nonlinear relationship, and the overall shape is concave. The closer the distance is from the outlet, the smaller the pore water pressure is. At the time t_1, the pore water pressure appears a transient negative pressure state when x is in the range of 4 to 10 mm. However, with the time goes on, the pore water pressure gradually increases, and after the flow pattern reaches stability (t_6), the pore water pressure has a linear relationship with the length of the seepage path, which is in line with the linear Darcy's law.

4. Conclusions

The permeability properties of red sandstone specimens after different high temperatures under the confining pressure can be well described by Darcy's law. The equivalent permeability coefficient is positively correlated with temperature and negatively correlated with confining pressure. In particular, the relationship between the equivalent permeability coefficient and confining pressure is a power function, and when the confining pressure increases from 10 to 30 MPa, the equivalent permeability coefficient decreased by 52.5–84.5%, while the equivalent permeability coefficient increases by 659.82 $\times 10^{-18}$ – 1388.49 $\times 10^{-18}$ m^2 as the temperature increases from 200 to 800°C.

There is a power function relationship between the mean pore size, porosity, and the equivalent permeability coefficient, and the mercury intake, mean pore diameter, and porosity increased by 2.7, 1.6, and 2.8 times, respectively,

when the temperature increased from 200 to 800°C. Moreover, the pore structure of red sandstone can be changed by high temperature, which makes the surface of red sandstone have more microcracks and pores and provides a channel for fluid migration.

At the initial moment, the pore water pressure surface gathered at the inlet, and the flow field in the model was disordered. As time went on, the pore water pressure surface expanded along the outlet direction, the spacing between the pore water pressure surfaces gradually expanded, and the streamlines within the pressure influence range became orderly. At this time, the pore water pressure and the seepage path length presented a nonlinear relationship. When the internal flow field of the model is stable and orderly, the fluid flow line is perpendicular to the pore water pressure surface, and the pore water pressure surface presents an equidistant distribution. In this case, the pore water pressure has a linear relationship with the seepage path length, which is in line with the linear Darcy's law.

Data Availability

The data used to support the findings of this study are included within the article.

Conflicts of Interest

The authors declare that they have no conflicts of interest to report regarding the present study.

Authors' Contributions

The manuscript was written through the contributions of all authors. All authors have given approval to the final version of the modified manuscript.

Acknowledgments

References

[1] X. F. Wang, C. G. Liu, S. J. Chen, L. Chen, K. Li, and N. Liu, "Impact of coal sector's de-capacity policy on coal price," *Applied Energy*, vol. 265, article 114802, 2020.

[2] Z. Li, H. Zhou, D. W. Hu, and C. Q. Zhang, "Yield criterion for rocklike geomaterials based on strain energy and CMP model," *International Journal of Geomechanics*, vol. 20, no. 3, article 04020013, 2020.

[3] C. Zhu, M. C. He, M. Karakus, X. B. Cui, and Z. G. Tao, "Investigating toppling failure mechanism of anti-dip layered slope due to excavation by physical modelling," *Rock Mechanics and Rock Engineering*, vol. 53, no. 11, pp. 5029–5050, 2020.

[4] J. Y. Wu, M. M. Feng, X. B. Mao et al., "Particle size distribution of aggregate effects on mechanical and structural properties of cemented rockfill: experiments and modeling,"

Construction and Building Materials, vol. 193, pp. 295–311, 2018.

[5] L. Wang, J. F. Liu, J. L. Pei, H. N. Xu, and Y. Bian, "Mechanical and permeability characteristics of rock under hydro-mechanical coupling conditions," *Environmental Earth Sciences*, vol. 73, no. 10, pp. 5987–5996, 2015.

[6] R. C. Liu, L. Y. Yu, and Y. J. Jiang, "Fractal analysis of directional permeability of gas shale fracture networks: a numerical study," *Journal of Natural Gas Science and Engineering*, vol. 33, pp. 1330–1341, 2016.

[7] W. A. M. Wanniarachchi, P. G. Ranjith, M. S. A. Perera, T. D. Rathnaweera, C. Zhang, and D. C. Zhang, "An integrated approach to simulate fracture permeability and flow characteristics using regenerated rock fracture from 3-D scanning: a numerical study," *Journal of Natural Gas Science and Engineering*, vol. 53, pp. 249–262, 2018.

[8] L. X. He, Q. Yin, and H. W. Jing, "Laboratory investigation of granite permeability after high-temperature exposure," *Processes*, vol. 6, no. 4, p. 36, 2018.

[9] Q. Yin, R. C. Liu, H. W. Jing, H. J. Su, L. Y. Yu, and L. X. He, "Experimental study of nonlinear flow behaviors through fractured rock samples after high-temperature exposure," *Rock Mechanics and Rock Engineering*, vol. 52, no. 9, pp. 2963–2983, 2019.

[10] Q. Yin, H. W. Jing, R. C. Liu, H. J. Su, L. Y. Yu, and G. S. Han, "Pore characteristics and nonlinear flow behaviors of granite exposed to high temperature," *Bulletin of Engineering Geology and the Environment*, vol. 79, no. 3, pp. 1239–1257, 2020.

[11] Y. Gao, R. C. Liu, H. W. Jing, W. Q. Chen, and Q. Yin, "Hydraulic properties of single fractures grouted by different types of carbon nanomaterial-based cement composites," *Bulletin of Engineering Geology and the Environment*, vol. 79, no. 5, pp. 2411–2421, 2020.

[12] Z. Li, H. X. Liu, Z. L. Dun, L. W. Ren, and J. J. Fang, "Grouting effect on rock fracture using shear and seepage assessment," *Construction and Building Materials*, vol. 242, article 118131, 2020.

[13] A. K. M. B. Alam, Y. Fujii, D. Fukuda, J. Kodama, and K. Kaneko, "Fractured rock permeability as a function of temperature and confining pressure," *Pure and Applied Geophysics*, vol. 172, no. 10, pp. 2871–2889, 2015.

[14] X. F. Liu, S. Y. Yuan, Y. Sieffert, S. Fityus, and O. Buzzi, "Changes in mineralogy, microstructure, compressive strength and intrinsic permeability of two sedimentary rocks subjected to high-temperature heating," *Rock Mechanics and Rock Engineering*, vol. 49, no. 8, pp. 2985–2998, 2016.

[15] Q. L. Ding, F. Ju, S. B. Song, B. Y. Yu, and D. Ma, "An experimental study of fractured sandstone permeability after high-temperature treatment under different confining pressures," *Journal of Natural Gas Science and Engineering*, vol. 34, pp. 55–63, 2016.

[16] M. Tao, Y. Yechao, C. Jie, and H. Yaoqing, "Investigation on the permeability evolution of gypsum interlayer under high temperature and triaxial pressure," *Rock Mechanics and Rock Engineering*, vol. 50, no. 8, pp. 2059–2069, 2017.

[17] Z. L. Ge, Q. Sun, and W. P. Li, "Temperature and pressure effect on permeability of Chinese sandstone: a review," *Acta Geodynamica et Geomaterialia*, vol. 15, no. 3, pp. 289–296, 2018.

[18] J. Y. Wu, M. M. Feng, B. Y. Yu, W. L. Zhang, X. Y. Ni, and G. S. Han, "Experimental investigation on dilatancy behavior of water-saturated sandstone," *International Journal of Mining Science and Technology*, vol. 28, no. 2, pp. 323–329, 2018.

[19] R. D. Dwivedi, R. K. Goel, V. V. R. Prasad, and A. Sinha, "Thermo-mechanical properties of Indian and other granites," *International Journal of Rock Mechanics and Mining Sciences*, vol. 45, no. 3, pp. 303–315, 2008.

[20] L. Griffiths, O. Lengline, M. J. Heap, P. Baud, and J. Schmittbuhl, "Thermal cracking in westerly granite monitored using direct wave velocity, coda wave interferometry and acoustic emissions," *Journal of Geophysical Research: Solid Earth*, vol. 123, no. 3, pp. 2246–2261, 2018.

[21] D. M. Freire-Lista, R. Fort, and M. J. Varas-Muriel, "Thermal stress-induced microcracking in building granite," *Engineering Geology*, vol. 206, pp. 83–93, 2016.

[22] S. Chaki, M. Takarli, and W. P. Agbodjan, "Influence of thermal damage on physical properties of a granite rock: porosity, permeability and ultrasonic wave evolutions," *Construction and Building Materials*, vol. 22, no. 7, pp. 1456–1461, 2008.

[23] Y. Ma, J. Hu, and G. Ye, "The pore structure and permeability of alkali activated fly ash," *Fuel*, vol. 104, pp. 771–780, 2013.

[24] S. W. Chen, C. H. Yang, and G. B. Wang, "Evolution of thermal damage and permeability of Beishan granite," *Applied Thermal Engineering*, vol. 110, pp. 1533–1542, 2017.

[25] Y. Gao, H. W. Jing, Z. F. Zhou, W. Q. Chen, M. du, and Y. du, "Reinforced impermeability of cementitious composites using graphene oxide- carbon nanotube hybrid under different water-to-cement ratios," *Construction and Building Materials*, vol. 222, pp. 610–621, 2019.

[26] G. H. Jiang, J. P. Zuo, T. Ma, and X. Wei, "Experimental investigation of wave velocity-permeability model for granite subjected to different temperature processing," *Geofluids*, vol. 2017, Article ID 6586438, 10 pages, 2017.

[27] C. J. Jia, W. Y. Xu, H. L. Wang, R. B. Wang, J. Yu, and L. Yan, "Stress dependent permeability and porosity of low-permeability rock," *Journal of Central South University*, vol. 24, no. 10, pp. 2396–2405, 2017.

[28] J. T. Zheng, L. G. Zheng, H. H. Liu, and Y. Ju, "Relationships between permeability, porosity and effective stress for low-permeability sedimentary rock," *International Journal of Rock Mechanics and Mining Sciences*, vol. 78, pp. 304–318, 2015.

[29] A. Kozusnikova and P. Konecny, "Influence of temperature on the permeability of rocks," *Geotechnique*, vol. 61, no. 12, pp. 1081–1085, 2011.

[30] W. L. Tian, S. Q. Yang, D. Elsworth, J. G. Wang, and X. Z. Li, "Permeability evolution and crack characteristics in granite under treatment at high temperature," *International Journal of Rock Mechanics and Mining Sciences*, vol. 134, p. 104461, 2020.

[31] C. E. Fairhurst and J. A. Hudson, "Draft ISRM suggested method for the complete stress-strain curve for the intact rock in uniaxial compression," *International Journal of Rock Mechanics and Mining Sciences*, vol. 36, no. 3, pp. 279–289, 1999.

[32] Q. Yin, H. W. Jing, and G. W. Ma, "Experimental study on mechanical properties of sandstone specimens containing a single hole after high-temperature exposure," *Géotechnique Letters*, vol. 5, no. 1, pp. 43–48, 2015.

[33] R. C. Liu, Y. J. Jiang, B. Li, and X. S. Wang, "A fractal model for characterizing fluid flow in fractured rock masses based on randomly distributed rock fracture networks," *Computers and Geotechnics*, vol. 65, pp. 45–55, 2015.

[34] C. Zhu, X. D. Xu, W. R. Liu et al., "Softening damage analysis of gypsum rock with water immersion time based on laboratory experiment," *IEEE Access*, vol. 7, pp. 125575–125585, 2019.

[35] R. W. Zimmerman, A. AL-Yaarubi, C. C. Pain, and C. A. Grattoni, "Non-linear regimes of fluid flow in rock fractures," *International Journal of Rock Mechanics and Mining Sciences*, vol. 41, no. 3, p. 384, 2004.

[36] Q. X. Meng, H. L. Wang, M. Cai, W. Y. Xu, X. Y. Zhuang, and T. Rabczuk, "Three-dimensional mesoscale computational modeling of soil-rock mixtures with concave particles," *Engineering Geology*, vol. 277, article 105802, 2020.

[37] Z. Li, S. G. Liu, W. T. Ren, J. J. Fang, Q. H. Zhu, and Z. L. Dun, "Multiscale laboratory study and numerical analysis of water-weakening effect on shale," *Advances in Materials Science and Engineering*, vol. 2020, Article ID 5263431, 14 pages, 2020.

[38] Q. S. Zhang, P. Li, G. Wang et al., "Parameters optimization of curtain grouting reinforcement cycle in Yonglian tunnel and its application," *Mathematical Problems in Engineering*, vol. 2015, Article ID 615736, 15 pages, 2015.